Submitted to Physical Review B, October 16, 2003.

Path Integral Monte Carlo Calculation of the Momentum Distribution of the Homogeneous Electron Gas at Finite Temperature

B. Militzer*
Geophysical Laboratory, Carnegie Institution of Washington, 5251 Broad Branch Road, NW, Washington, DC 20015

E. L. Pollock†
Lawrence Livermore National Laboratory, University of California, Livermore, CA 94550

D. M. Ceperley‡
Department of Physics, National Center for Supercomputing Applications, University of Illinois at Urbana-Champaign, Urbana, IL 61801

Path integral Monte Carlo (PIMC) simulations are used to calculate the momentum distribution of the homogeneous electron gas at finite temperature. This is done by calculating the off-diagonal elements of the real-space density matrix, represented in PIMC by open paths. It is demonstrated how the restricted path integral Monte Carlo methods can be extended in order to deal with open paths in fermionic systems where a sign problem is present. The computed momentum distribution shows significant deviations for strong correlation from free fermion results but agrees with predictions from variational methods.

I. INTRODUCTION

The momentum distribution is one of the fundamental properties of a quantum system. It can be directly measured by inelastic scattering or by studying the trajectories of particles. The first method has been used to determine the condensate fraction in liquid helium while the latter was used to demonstrate that Bose-Einstein condensation of supercooled alkali atoms in magnetic traps had been achieved.

In this article, we calculate the momentum distribution of fermion systems at finite temperature with path integral Monte Carlo (PIMC). The results show how the fermionic momentum distribution evolves as a function of temperature. At a temperature much higher than the Fermi temperature, T_F, the fluid has a Maxwell-Boltzmann momentum distribution and with decreasing temperature, the Pauli exclusion principle becomes more important giving rise to a Fermi surface. While it is very simple to study this cross-over in noninteracting systems, interparticle interactions require a much more sophisticated description.

Here we compute the effect of interactions of the momentum distribution at finite temperature using fermion restricted path integral Monte Carlo simulations. To determine the needed off-diagonal density matrix elements we need to perform simulations with open paths. We compute these properties for the homogeneous electron gas and demonstrate how increased correlation effects alter the momentum distribution at different temperatures.

*Electronic address: militzer@gl.ciw.edu
†Electronic address: pollock1@llnl.gov
‡Electronic address: ceperley@uiuc.edu

II. PATH INTEGRAL MONTE CARLO

We now give a brief review of the PIMC simulation technique for fermions and of the restricted path method. In PIMC calculations of the diagonal density matrix each particle is represented by a *closed path* in imaginary time. Following the procedure developed for bosonic systems [1], we extend fermionic PIMC to estimate off-diagonal density matrix elements needed for the momentum distribution. This requires one of the particle paths to be *open*. Special emphasis will be placed on how the path restriction is applied to open paths and how the Monte Carlo sampling is affected.

A. Restricted paths technique

The thermodynamic properties of a quantum many-body system can be derived from the thermal density, $\hat{\rho} = e^{-\beta\hat{\mathcal{H}}}$ with $\beta = 1/k_B T$. For the purpose of performing Monte Carlo simulations, we express this operator in position-space,

$$\rho(\mathbf{R}, \mathbf{R}'; \beta) \equiv \langle \mathbf{R} | \hat{\rho} | \mathbf{R}' \rangle = \sum_s e^{-\beta\epsilon_s} \Psi_s^*(\mathbf{R}) \Psi_s(\mathbf{R}') , \tag{2.1}$$

where Ψ_s are the many-body eigenfunctions and ϵ_s the corresponding eigenvalues. $\mathbf{R} = \{\mathbf{r}_1, \ldots, \mathbf{r}_N\}$ represents a set of coordinates of N particles in d dimensions. The density matrix of a bosonic (B) or fermionic (F) system, $\rho_{\mathrm{B/F}}(\mathbf{R}, \mathbf{R}'; \beta)$, can be constructed from the density matrix for distinguishable particles by a sum of permutations, $\mathcal{P}$, to project out states of the corresponding symmetry,

$$\rho_{\mathrm{B/F}}(\mathbf{R}, \mathbf{R}'; \beta) = \frac{1}{N!} \sum_{\mathcal{P}} (\pm 1)^{\mathcal{P}} \rho_{\mathrm{D}}(\mathbf{R}, \mathcal{P}\mathbf{R}'; \beta) , \tag{2.2}$$

where $(\pm 1)^{\mathcal{P}}$ denotes the sign of the permutation. Using the operator identity, $e^{-\beta\hat{\mathcal{H}}} = (e^{-\tau\hat{\mathcal{H}}})^M$, the density matrix at temperature T can be expressed in terms of density matrices at a higher temperature MT. This leads to a path integral with M steps in imaginary time of size $\tau = \beta/M$,

$$\rho_{\mathrm{B/F}}(\mathbf{R},\mathbf{R}';\beta) = \frac{1}{N!}\sum_{\mathcal{P}}(\pm 1)^{\mathcal{P}}\int\!\cdots\!\int \mathbf{dR}_1\,\mathbf{dR}_2\ldots\mathbf{dR}_{M-1}$$
$$\rho_{\mathrm{D}}(\mathbf{R},\mathbf{R}_1;\tau)\,\rho_{\mathrm{D}}(\mathbf{R}_1,\mathbf{R}_2;\tau)\ldots\rho_{\mathrm{D}}(\mathbf{R}_{M-1},\mathcal{P}\mathbf{R}';\tau)$$
$$= \frac{1}{N!}\sum_{\mathcal{P}}(\pm 1)^{\mathcal{P}}\int_{\mathbf{R}\to\mathcal{P}\mathbf{R}'}\mathbf{dR}_t\;\; e^{-S[\mathbf{R}_t]}\,, \qquad (2.3)$$

where S represents the "action" of the path $\mathbf{R}_t$ beginning at $\mathbf{R}$ and ending at $\mathcal{P}\mathbf{R}'$. Here we use the pair density matrix for the link actions: $\rho_{\mathrm{D}}(\mathbf{R}_1,\mathbf{R}_2;\tau)$. For bosonic many-body systems, the integrand is nonnegative and this expression can be efficiently evaluated using Monte Carlo techniques [1]. In the case of fermions, a straightforward evaluation of this expression is impractical because the cancellation of many positive and negative terms of the same order leading to numerically inefficient computation in the low temperature, many-fermion limit. While one can still use this expression to numerically study systems of a few fermions, the efficiency rapidly decays with increasing number of particles and decreasing temperature, $\sim e^{-\beta N}$. This is referred to as the *fermion sign problem.*

Ceperley [2–4] has shown that the fermion sign problem in imaginary time path integrals can be solved by *restricting* the path integration to a subvolume of the entire path space. Let us define the *nodes* of the fermion many-body density matrix as the surface where $\rho_F(\mathbf{R},\mathbf{R}';t) = 0$. The nodes are used to confine the paths $\mathbf{R}(t)$ to regions where the density matrix is nonzero, $\rho_F(\mathbf{R}^*,\mathbf{R}(t);t) \neq 0$. $\mathbf{R}^*$ is called the *reference point* and defines the region in $\{\mathbf{R},t\}$ space ($\Upsilon(\mathbf{R}^*;t)$) where the path is allowed to be. The fermionic density matrix is then given by the restricted path integral,

$$\rho_F(\mathbf{R}^*,\mathbf{R}';\beta) = \frac{1}{N!}\sum_{\mathcal{P}}(-1)^{\mathcal{P}}\int_{\mathbf{R}^*\to\mathcal{P}\mathbf{R}'\in\Upsilon(\mathbf{R}^*;t)}\mathbf{dR}_t\;\; e^{-S[\mathbf{R}_t]}\quad, \qquad (2.4)$$

where one sums and integrates over all paths that never cross the nodal boundaries. By introducing this restriction, one effectively cancels all negative and some positive contributions to the trace of density matrix. Complete cancellation of all negative terms, however, is only reached on the diagonal of the density matrix. Off the diagonal, negative contributions also enter the restricted path integral, as will be illustrated below. In either case, the restriction gives rise to an efficient numerical algorithm that scales favorably with increasing number of particles, similar to that for bosons.

The expression in Eq. 2.4 is exact as long as the restriction is exact [2]. The exact density matrix is only known in a few cases, e.g. for noninteracting particles. In practice, one introduces a *trial* density matrix $\rho_{\mathrm{T}}(\mathbf{R},\mathbf{R}';\beta)$ that provides approximate fermion nodes which introduces an approximation in computed observables. However, for many systems this technique has worked well.

The simplest approximation for the trial density matrix $\rho_T(\mathbf{R},\mathbf{R}';\beta)$ is a Slater determinant of single particle density matrices,

$$\rho_T(\mathbf{R},\mathbf{R}';\beta) = \begin{vmatrix} \rho^{[1]}(\mathbf{r}_1,\mathbf{r}'_1;\beta) & \ldots & \rho^{[1]}(\mathbf{r}_N,\mathbf{r}'_1;\beta) \\ \ldots & \ldots & \ldots \\ \rho^{[1]}(\mathbf{r}_1,\mathbf{r}'_N;\beta) & \ldots & \rho^{[1]}(\mathbf{r}_N,\mathbf{r}'_N;\beta) \end{vmatrix}\,. \qquad (2.5)$$

For a homogeneous Fermi liquid, such as the electron gas, the single particle density matrices are:

$$\rho_0^{[1]}(\mathbf{r},\mathbf{r}';\beta) = (4\pi\lambda\beta)^{-d/2}\exp\left\{-\frac{(\mathbf{r}-\mathbf{r}')^2}{4\lambda\beta}\right\}\quad, \qquad (2.6)$$

where $\lambda = \hbar^2/2m$. For temperatures above the Fermi energy, where exchange is small, the nodal surfaces of this determinant are accurate. At decreasing temperature, interaction effects become more important and consequently the error from employing free particle nodes increases. (Note, however, that the nodes are second order in the interaction.) One can improve the nodal approximation by using the dual-reference point method [4]. In this approach, the nodal restriction is $\rho_T(\mathbf{R}(t),\mathbf{R}^*;t^*) \neq 0$ where $t^* = \min(t,\beta-t)$ is the smaller imaginary time separation from the reference point. The dual-reference point method will be used throughout this work.

How sensitive the derived results are to the accuracy of the nodes can depend on the interactions in a particular system. Generally, one expects free particle nodes to work well at high temperature and when correlation effects are weak. Also, when particles are localized like the electrons in molecular hydrogen or particles in a Wigner crystal, the effect of the nodes is reduced and nodal restriction is unimportant. One can improve nodal surfaces in several ways. For example, one can derive the nodes from a variational density matrix [5], by treating the interactions with Hartree-Fock. Or, one can use backflow in the density matrix to account for interaction effects [2, 4].

Consider the calculation of an observable, $\mathcal{O}$, diagonal in $\mathbf{R}$ space such as the pressure, kinetic, potential and internal energy as well as pair correlation functions:

$$\langle\mathcal{O}\rangle = \frac{1}{\mathcal{Z}}\int\mathbf{dR}\;\rho(\mathbf{R},\mathbf{R};\beta)\;\langle\mathbf{R}|\,\mathcal{O}\,|\mathbf{R}\rangle\;, \qquad (2.7)$$

$$\mathcal{Z} = \int\mathbf{dR}\;\rho(\mathbf{R},\mathbf{R};\beta)\quad. \qquad (2.8)$$

Such computations require only simulations with closed paths, beginning at a point $\mathbf{R}$ and ending at its permutation, $\mathcal{P}\mathbf{R}$. The restriction eliminates all contributions from odd permutations that would enter with a negative weight because their paths would violate the nodal constraint an odd number of times.

B. Computation of the momentum distribution

The single-particle momentum distribution for N_σ particles in spin state σ is defined as,

$$n(\mathbf{k}) = \frac{(2\pi\hbar)^d}{\Omega}\left\langle \sum_{j=1}^{N_\sigma} \delta(\hat{\mathbf{p}}_j - \hbar\mathbf{k}) \right\rangle \ , \qquad (2.9)$$

with the normalization for a finite system and in the thermodynamic limit respectively given by,

$$\sum_{\mathbf{k}} n(\mathbf{k}) = N_\sigma \quad , \quad \frac{\Omega}{(2\pi)^d}\int \mathbf{dk}\ n(\mathbf{k}) = N_\sigma \ . \qquad (2.10)$$

Inserting complete sets of states and using $\langle \mathbf{R}|\mathbf{P}\rangle = e^{-i\mathbf{R}\cdot\mathbf{P}/\hbar}/(2\pi\hbar)^{Nd/2}$, one finds,

$$n(\mathbf{k}) = \frac{1}{\mathcal{Z}\Omega}\int \mathbf{dR dR' dP}\ \langle \mathbf{R}|\hat{\rho}|\mathbf{R}'\rangle \frac{e^{i\mathbf{P}\cdot(\mathbf{R}-\mathbf{R}')/\hbar}}{(2\pi\hbar)^{(N-1)d}} \sum_{j=1}^{N_\sigma} \delta(\mathbf{p}_j - \hbar\mathbf{k})$$

$$= \frac{N_\sigma}{\mathcal{Z}\Omega}\int \mathbf{dR dr}_1' e^{i(\mathbf{r}_1 - \mathbf{r}_1')\cdot\mathbf{k}} \rho(\mathbf{r}_1, \ldots, \mathbf{r}_N, \mathbf{r}_1', \mathbf{r}_2, \ldots, \mathbf{r}_N).$$

The last line follows from the equivalence of all the particles assuming particle 1 has spin σ. Consequently, $n(\mathbf{k})$ is given by the Fourier transform of the single-particle reduced density matrix (SPRDM), $n(\mathbf{s})$,

$$n(\mathbf{k}) = \frac{N_\sigma}{\Omega}\int \mathbf{ds}\ e^{-i\mathbf{ks}}\ n(\mathbf{s}) \ , \qquad (2.11)$$

$$n(\mathbf{s}) = \frac{1}{\mathcal{Z}}\int \mathbf{dR}\ \rho(\mathbf{r}_1, \mathbf{r}_2, \ldots, \mathbf{r}_N\ ,\ \mathbf{r}_1 + \mathbf{s}, \mathbf{r}_2, \ldots, \mathbf{r}_N) \ .$$

Note that $n(s=0) = 1$ from the definition.

Classical particles have a Maxwellian momentum distribution with

$$n(\mathbf{k}) = \frac{N_\sigma}{\Omega}(4\pi\lambda\beta)^{d/2}\exp\left\{-\beta\lambda\mathbf{k}^2\right\} \ , \qquad (2.12)$$

$$n(\mathbf{s}) = \exp\left\{-\frac{\mathbf{s}^2}{4\lambda\beta}\right\} \ . \qquad (2.13)$$

For an ideal Fermi gas in 3 dimensions at $T = 0$, the momentum distribution (for one spin state) is a Fermi function,

$$n(\mathbf{k}) = \begin{cases} 1 & \text{for} \quad k \le k_F \\ 0 & \text{for} \quad k > k_F \end{cases} \quad \text{with} \quad k_F = (6\pi^2 N_\sigma/\Omega)^{1/3}$$

$$n(\mathbf{s}) = 3/x^3\left[\sin x - x\cos x\right] \ \text{with} \ x = s\,k_F \quad .$$

Hence, the free fermion SPRDM decays to zero as $\cos(s\,k_F)/s^2$ at zero temperature.

The function $n(\mathbf{s})$ can be computed from PIMC simulations with one open path, where the vector $\mathbf{s}$ is the separation of the two open ends. Methods developed for bosonic systems [1], such as liquid ^{4}He, carry over directly to fermion path integrals except for the considerations having to do with the nodal restrictions. In the simulations, $n(s)$ is obtained as a histogram, in which one enters the observed separations of the open ends weighted with the sign of the permutation. The discussion in the previous subsection concerning the elimination of odd permutations holds for diagonal paths. Off-diagonal paths with odd permutations do contribute to the Monte Carlo averages with a negative weight. At separations where $n(s)$ is negative, odd permutations outweigh even permutations. The algebraic decay of $n(\mathbf{s})$ requires long exchange cycles, of the order of the number of particles. In restricted PIMC, there is a direct relation [4] between long exchange cycles and the discontinuity of $n(k)$ at $k = k_F$.

C. Example of two free fermions

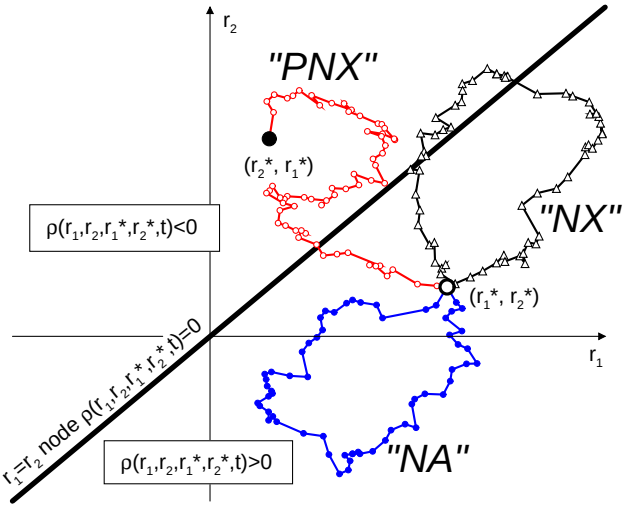

FIG. 1: Illustration of the three different types of paths for two free fermions all starting at a given reference point $(\mathbf{r}_1^*, \mathbf{r}_2^*)$. A node-avoiding ("NA"), a node-crossing ("NX") as well as a permuting and consequently node-crossing path ("PNX") are shown in the $(\mathbf{r}_1, \mathbf{r}_2)$ plane. The thick solid line indicates the node.

In order to illustrate the restricted path integral technique, we discuss the simplest fermionic system: the case of two free fermions with the same spin without boundaries. The density matrix $\rho_T(\mathbf{r}_1, \mathbf{r}_2, \mathbf{r}_1^*, \mathbf{r}_2^*; \beta)$ (Eq. 2.5) is positive when

$$(\mathbf{r}_1 - \mathbf{r}_2)\cdot(\mathbf{r}_1^* - \mathbf{r}_2^*) > 0. \qquad (2.14)$$

The nodal surface is the hyperplane $\mathbf{r}_1 = \mathbf{r}_2$ at all temperatures as illustrated in Fig. 1. This figure also shows the three types of paths that contribute to the trace of the density matrix. Since we only consider diagonal density matrix elements in this figure, the path starting at the reference point, $(\mathbf{r}_1^*, \mathbf{r}_2^*)$, can either return to its origin or to the only possible permutation of it, $(\mathbf{r}_2^*, \mathbf{r}_1^*)$.

In restricted PIMC, only node-avoiding paths, labeled "NA", contribute. In the case of two particles, the restriction prohibits any permutation. In case of the direct (unrestricted) fermion method, nonpermuting path that

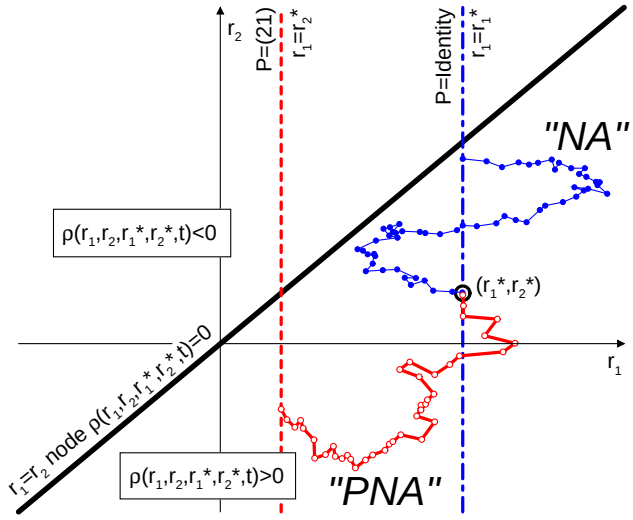

FIG. 2: Illustration of node-avoiding paths that contribute to *off-diagonal* density matrix elements for two free fermions. All start at the reference point $(\mathbf{r}_1^*, \mathbf{r}_2^*)$. Shown are paths with one open end at r_2. The dot-dashed line indicates possible end points for nonpermuting paths [$\mathbf{r}_1 = \mathbf{r}_1^*$, labeled "NA"]. In contrast to on-diagonal matrix elements shown in Fig. 1, here, we find permuting but node-avoiding paths with end points on the dashed line [$\mathbf{r}_1 = \mathbf{r}_2^*$, labeled "PNA"] that represent negative contributions to the density matrix.

cross the nodes ("NX") and those that avoid it, enter with a positive sign. Permuting paths ("PNX") now also enter with a negative weight because of the $(-1)^{\mathcal{P}}$ factor. For bosons, permuting and nonpermuting paths enter a with positive weight.

In order to compute the momentum distribution for two particles, one would perform simulations with one open and one closed path. Fig. 2 illustrates such paths in the $(\mathbf{r}_1, \mathbf{r}_2)$ plane. For simplicity, only node-avoiding paths that begin at $(\mathbf{r}_1^*, \mathbf{r}_2^*)$ and have an open end at $\mathbf{r}_2$ are shown. Under these restrictions, only two types of paths remain: (i) Nonpermuting paths with $\mathbf{r}_1 = \mathbf{r}_1^*$ and $\mathbf{r}_2 \neq \mathbf{r}_2^*$. Path 1 would appear as a closed polymer while path 2 would be open. (ii) A new category appears: node-avoiding but permuting paths with $\mathbf{r}_1 = \mathbf{r}_2^*$ and $\mathbf{r}_2 \neq \mathbf{r}_1^*$. In the case of closed paths, the nodal restriction eliminates permutations because the final point $(\mathbf{r}_2^*, \mathbf{r}_1^*)$ lies on the other side of the node. However, for open paths, many final points for permuting paths are possible (see dashed line in Fig. 2) because path 2 does not have to end at the beginning of path 1.

With increasing number of fermions, it is difficult to illustrate the nodal constraint graphically. However, this is not a computational difficulty since one can easily verify the sign of the Slater determinant for any proposed path to see if it is node-avoiding.

D. Monte Carlo sampling with open paths

To apply the restricted path integral to open paths, one first has to decide at which time slice one opens the paths, relative to the reference point, assumed to be at $t = 0$. Using the dual reference point method, one can put the open ends at $t = 0$, or at $t = \beta/2$. We used the latter choice because it is more symmetrical and it avoids the singular behavior of the fermion density matrices as $t \to 0^+$.

To move the open and closed paths in the presence of nodal constraints, one first picks a time interval of size 2^l in which the paths will be modified where l is the number of levels in the bisection method [1]. If it is chosen too large, most trial moves will be rejected. If it is too small, the paths diffuse too slowly. The optimal choice depends on strength of the interactions and on the fermion degeneracy. After selecting the time interval, one uses the heat-bath algorithm (see [1] for details) to sample a particular cyclic permutation of moving particles. Then one proceeds with a bisection method for all l levels in order to determine the positions of the moving particles at each time slice. In this study, the sampling probabilities are taken from the free particle density matrix. For a closed path connecting points $\mathbf{r}_1$ and $\mathbf{r}_2$, this becomes,

$$T_l(\mathbf{r}) = (2^l \pi \lambda \tau)^{d/2} \exp\left\{ -\frac{(\mathbf{r} - \mathbf{r}_{\rm m})^2}{2^l \lambda \tau} \right\} \quad , \qquad (2.15)$$

where $\mathbf{r}_{\rm m}$ is the mid point $(\mathbf{r}_1 + \mathbf{r}_2)/2$. For strongly interacting systems, a better sampling efficiency has been reached by adding a drift and a covariance term [1]. For an open end, which is only connected to one point $\mathbf{r}_1$, the free particle sampling probability is,

$$T_l(\mathbf{r}) = (4^l \pi \lambda \tau)^{d/2} \exp\left\{ -\frac{(\mathbf{r} - \mathbf{r}_1)^2}{4^l \lambda \tau} \right\} \quad . \qquad (2.16)$$

The pair action, $u(\mathbf{R}, \mathbf{R}'; \beta) = -\log[\rho(\mathbf{R}, \mathbf{R}'; \tau)/\rho_0(\mathbf{R}, \mathbf{R}'; \tau)]$, is then used to determine whether a particular configuration will be rejected or temporarily accepted.

As a final step, one verifies if the nodal constraint is satisfied at each time slice. Otherwise, the proposed configuration is rejected. For fermion simulations with only closed paths, one can eliminate odd permutation moves because they would inevitably violate the nodes. In the presence of open paths, this is not true; otherwise we would not get the negative pieces of the density matrix. The node-avoiding condition for each time slice is still the same, $\rho_T(\mathbf{R}(t), \mathbf{R}^*; \min(t, \beta - t)) > 0$. The following two conditions can be used to eliminate paths violating the nodal constraint: (a) It is impossible to permute an even number of closed paths while keeping all other particle coordinates fixed. (b) It is impossible to permute an open and a closed path in a move that does not change the time slice with the open ends. It should be noted that the rules are only employed to improve the efficiency. Paths violating these conditions would be rejected anyway when the nodal constraints are enforced.

TABLE I: Kinetic and potential energy, K and V, per particle in units of Hartrees are tabulated for $r_s = 4$ and 40 for the spin polarized ($N_\uparrow = 0$) and unpolarized homogeneous electron gas ($N_\uparrow = N_\downarrow$).

$\frac{T_F}{T}$	$N_\uparrow$	$N_\downarrow$	$K[r_s=4]$	$V[r_s=4]$	$K[r_s=40]$	$V[r_s=40]$
1	33	0	0.2961(6)	–0.1513(1)	0.00354(2)	–0.019553(4)
2	33	0	0.177(1)	–0.16413(6)	0.002605(6)	–0.019774(2)
4	33	0	0.144(4)	–0.16997(5)	0.00237(1)	–0.019826(2)
8	33	0	0.143(8)	–0.17223(6)	0.00232(3)	–0.019834(2)
16	33	0	0.14(1)	–0.17341(4)	0.00227(4)	–0.019834(4)
1	33	33	0.1930(5)	–0.15574(9)	0.002859(4)	–0.019715(2)
2	33	33	0.123(1)	–0.1627(1)	0.002389(5)	–0.019789(3)
4	33	33	0.105(3)	–0.1636(1)	0.00230(1)	–0.019803(2)
8	33	33	0.101(6)	–0.1632(2)	0.00227(3)	–0.019803(2)
16	33	33	0.100(8)	–0.1631(2)	0.00232(5)	–0.019797(6)

The SPRDM is proportional to distribution of $\mathbf{s}$, the separation of the two ends. Configurations with an odd permutation contribute negatively. For a finite homogeneous system, $n(\mathbf{s})$ is only a function of $|\mathbf{s}|$. However, in a periodic but finite simulation cell, there is a dependence on the orientation of $\mathbf{s}$ with respect to the cell boundaries. In all following results, $n(\mathbf{s})$ will be spherically averaged. However, for the computation of the momentum distribution, $n(\mathbf{k}) \propto \langle e^{i\mathbf{k}\mathbf{s}} \rangle$, the angular dependence of $n(\mathbf{s})$ is important. We compute $n(\mathbf{k})$ directly during the Monte Carlo simulation for a reasonable number of $\mathbf{k}$ vectors, to avoid storing the d dimensional function $n(\mathbf{s})$.

The normalization of $n(s)$, is not determined *a priori* with a single PIMC run. We use the same method developed for the bosonic superfluid helium. The normalization is determined by its value at $n(s=0) = 1$. A difficulty arises from the fact that the probability that the two ends have a distance less than s scales as s^d in d dimensions and error bars accordingly increase for small s as $s^{-d/2}$. To smooth the errors, we fit the observed histogram of end-to-end separations to a function of the form:

$$\lim_{s\to 0} n_{\rm MC}(s) = \xi_1 \left[1 - \frac{\langle K \rangle}{\lambda d} s^2 + \xi_2 s^4\right] \quad , \qquad (2.17)$$

for the unknown parameters ξ_1 and ξ_2. Here K is the kinetic energy derived from a separate simulation with only closed paths. The specific values are given in Table I together with potential energy, V. The internal energy can be obtained by adding $K + V$ and pressure for coulomb systems, follows from the virial theorem, $3P\Omega = 2K + V$. The fit then determines the normalization constant ξ_1 of the momentum distribution. To further reduce the error bars of $n(s)$, we enhanced the frequency of moving the open ends by selecting the open path more often and also by moving the slice with the open ends more frequently.

III. RESULTS

We determined the momentum distribution of the homogeneous electron gas at three different conditions.

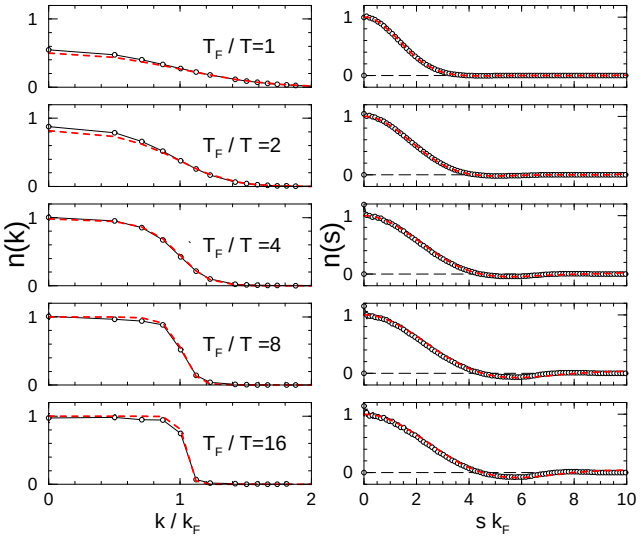

FIG. 3: The left panels show the momentum distributions $n(k)$ from PIMC simulations (circles) with 33 spin polarized electrons for different temperatures at ($r_s = 4$). For $T \geq T_F/4$, the population of low momentum states is enhanced compared with the corresponding ideal Fermion results (dashed lines), which leads to a lowering of kinetic energy ($K < K_0$). The right panel shows the corresponding off-diagonal density matrix elements $n(r)$. With decreasing temperature, a negative region near $sk_F = 5.8$ is apparent.

First, we study the spin polarized electron gas at a density of $r_s = 4$, which corresponds to the electron density of a low density metal such as sodium. The computed momentum distribution turns out to be similar to an ideal Fermi gas. Secondly, we calculated $n(k)$ for spin polarized electron gas at a much lower density of $r_s = 40$, where correlation effects are very large and significant deviations from free particle behavior are found. Finally, we present results for the unpolarized electron gas at $r_s = 40$ where correlation effects are even more important. For all three conditions, we have computed the momentum distribution for a series of different temperatures ranging from $1 \leq T_F/T \leq 16$. We compare with results from zero temperature quantum Monte Carlo simulations.

Fig. 3 shows the momentum distribution for spin polarized electron gas as a function of temperature. In the limit of high temperature $T \gg T_F$, fermion effects become less important and one recovers the classical Maxwell-Boltzmann distribution. With decreasing temperature, one finds that population of low momentum states with $k < k_F$ increases until it reaches 1, the maximum allowed by the Pauli exclusion principle. Simultaneously, the slope at the Fermi wave vector becomes increasingly steep. We do not exactly recover the limit of ideal Fermi function in Eq. 2.14, because of finite size effects. The system size we used, $N = 33$ at $T = T_F/16$, is already a demanding computation, in part because we used a time step of $\tau = 1/32T_F$ needed to enforce the nodal constraint accurately along the paths but requiring simulations with up to 384 time slices. Notice that at

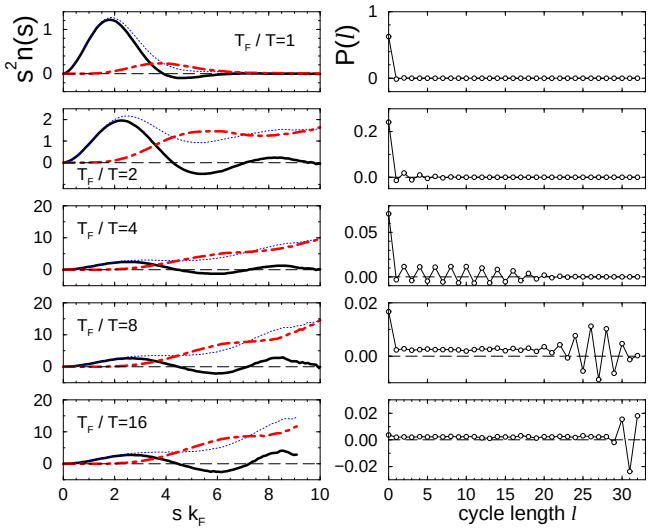

FIG. 4: The left column shows the distribution of the open ends, $n(s)$ multiplied by the volume element s^2 (solid lines) for a system of 33 spin polarized electrons for $r_s = 4$ at different temperatures (see corresponding Fig. 3). The dash-dotted lines indicate the distribution of paths that enter with a negative sign. Their contribution vanishes more quickly for small s because they do not contribute to diagonal density matrix elements. The dashed lines indicate the distribution of positive contributions. The right column shows the distribution of permutation cycles as a function of cycle length l times the weight of the overall permutation.

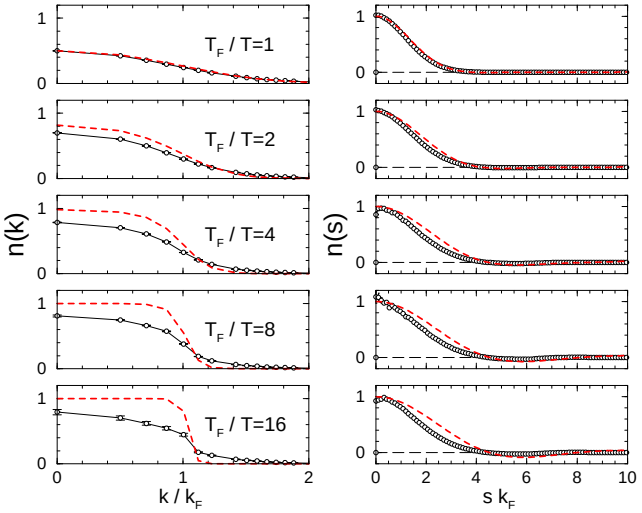

FIG. 5: Momentum distribution $n(k)$ and off-diagonal density matrix $n(r)$ for the spin polarized electron gas at $r_s = 40$ from simulations with 33 particles. Deviations from the ideal Fermion results are increased compared to Fig. 3 (see description and line styles there) due to increased correlation effects.

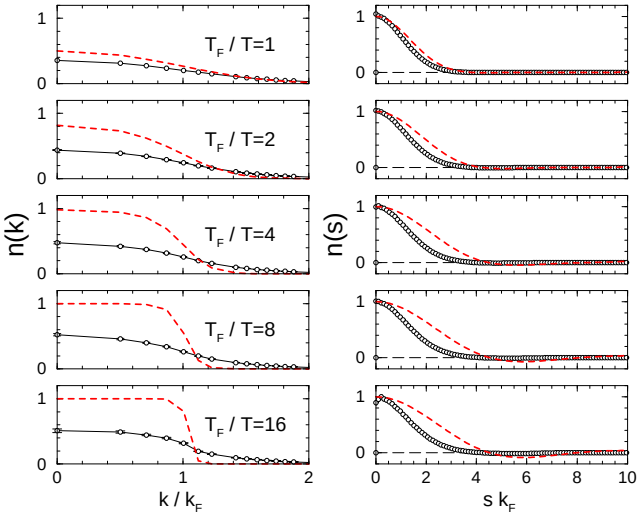

FIG. 6: Momentum distribution $n(k)$ and off-diagonal density matrix $n(r)$ function for the unpolarized electron gas at $r_s = 40$ from simulations with 66 particles. Correlation effects are enhanced compared to Figs. 3 and 5 (see description and line styles there).

$T = T_F/16$ there are still small but nonnegligible thermal excitations of states above k_F present. The correlation effects, absent for free particles, are small but nevertheless significant. At high temperature, the interactions lead to an increased population of low momentum states resulting in a lowering of the total kinetic energy. The reason for this effect is that the entropy is the dominant part of the free energy at high temperature. Interactions can lower the entropy which also leads to a lowering of the kinetic energy. This effect has been discussed in detail in [6]. At low temperature, the free energy is dominated by the interaction term and the kinetic energy is always higher than the corresponding ideal value. As a result, even at $T = 0$, states above the k_F are populated. According to Migdal's theorem [7], as long as the system remains a Fermi liquid, the discontinuity at k_F remains, but the step size is reduced compared to the free fermion value.

We have shown the SPRDM $n(s)$ on the right side of Fig. 3; they are very close to those of free particles at this density. However, in the more correlated systems, discussed later, significant deviations from the ideal behavior are found. At high temperature, (in the classical limit) $n(s)$ is dominated by a single Gaussian. With decreasing temperature, a shallow negative region develops around $sk_F = 5.8$. At $sk_F = 7.25$, $n(s)$ becomes positive again and exhibits a maximum at $sk_F = 8$. Further oscillations cannot be identified for this system size.

Fig. 4 shows the distribution of positive and negative contribution of the SPRDM. (The contribution to $s^2 n(s)$ is shown.) At small separation, $n(s)$ is dominated by the positive contribution because negative terms are prevented by the restriction since the paths become diagonal in this limit. The negative region near $sk_F = 5.8$ develops because two particle permutations occur with increasing probability for temperatures $T \leq T_F$. Such open paths can spread out further than single open paths and therefore start to dominate at larger s. As the temperature

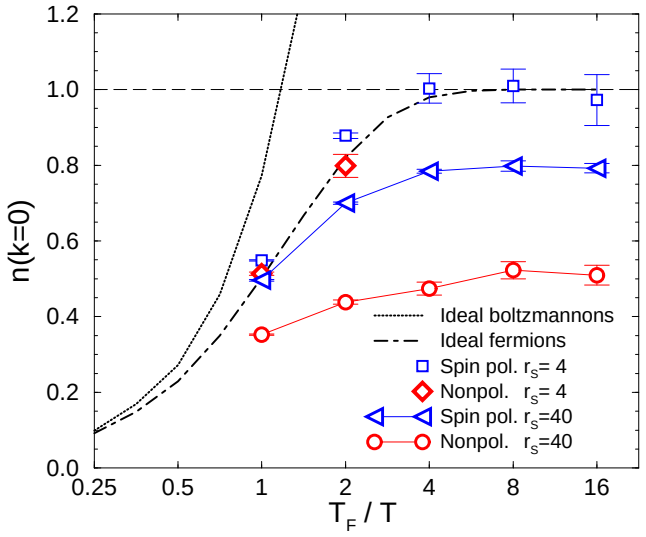

FIG. 7: The temperature dependence of the population of the zero momentum state, $n(k=0)$, is shown for two densities ($r_s = 4$ and 40) of the fully spin polarized electron gas (from PIMC simulations with 33 particles) and for the nonpolarized case (simulations with 66 particles).

is decreased further below T_F, longer and longer permutation cycles contribute to $n(s)$. The magnitude of positive and negative contributions increases with s but each function dominates for different separations giving rise to the oscillatory behavior of the total $n(s)$ function, which is expected from the zero temperature result.

Fig. 4 also shows the probability of finding a permutation cycle times the overall sign as a function of the cycle length. At high temperature the thermal De Broglie wave length, $\lambda_{\rm th}^2 = 4\pi\lambda\beta$, is short compared to the interparticle spacing, which makes the longer permutation cycles occur with small probability. With decreasing temperature, longer permutations occur more frequently and the cycle distribution approaches a positive constant. The occurrence of a particular cycle length is no longer correlated with total permutation, and overall there are more positive than negative total permutations. The difference gets smaller as the negative contributions become more important at an even lower temperature. This distribution shows oscillation for the largest occurring cycle lengths since if such a long cycle occurs it is unlikely there is also another permutation cycle that can alter the total sign of the permutation.

Fig. 5 shows the $n(k)$ and $n(s)$ functions for the spin polarized electron gas at a much lower density of $r_s = 40$. Under these conditions, the particles are significantly more correlated and their behavior differs substantially from free fermions. As a result, the momentum distribution is much more spread out leading to the population of higher momentum states. The total kinetic energy is clearly above the corresponding ideal value. In the low temperature limit, the population of the $k = 0$ state reaches a value of only about 0.8 relative to free particles. The $n(s)$ distribution is shifted to smaller s values indicating that the paths are more localized due to the repulsive interactions.

Fig. 6 shows the corresponding results for the unpolarized electron gas with 66 electrons. These simulations are comparatively easier than simulations at higher density because the interactions lead to some localization and cut down on the number of long permutation cycles which give a fluctuating sign. Simulations of a correlated system are therefore less demanding than that of weakly interacting particles.

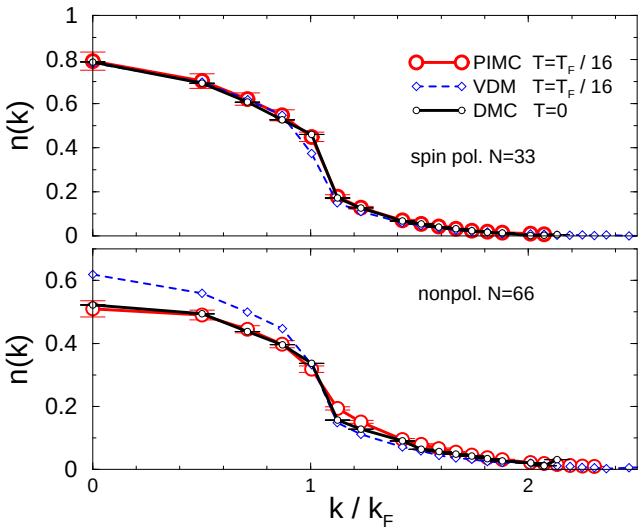

FIG. 8: Comparison of the momentum distribution for $r_s = 40$ at $T = T_F/16$ computed with PIMC, VDM and ground state diffusion Monte Carlo (DMC) calculations at $T = 0$. The upper graph shows results from simulation with 33 spin polarized electrons, the lower graph represents the unpolarized case with 66 particles.

In Fig. 7, the occupation of the zero momentum state is plotted as a function of temperature. At high temperature, all curves converge to the free particle result. Simulations of the spin polarized electron gas at $r_s = 4$ are above the ideal result for high temperatures underlining the lowering of the kinetic energy. For low temperatures, they converge to the ideal value of 1 within the error bars. The graph also shows that the low density results converge to a ground state limit as well.

In Fig. 8, we compare PIMC results and variational density matrix calculations (VDM) [8] at $T = T_F/16$ with the ground state momentum distribution derived from diffusion Monte Carlo (DMC) simulations using backflow nodes [9] (For additional DMC results see [10]). The agreement between PIMC and DMC is excellent for both spin polarizations considered here. Only for the nonpolarized case, one observes some very small deviations around $k \approx k_F$, an indication of thermal excitation present. Fig. 8 for the spin polarized case also shows good agreement with a VDM calculation using the free particle density matrix (Eq. 2.5) multiplied by a temperature

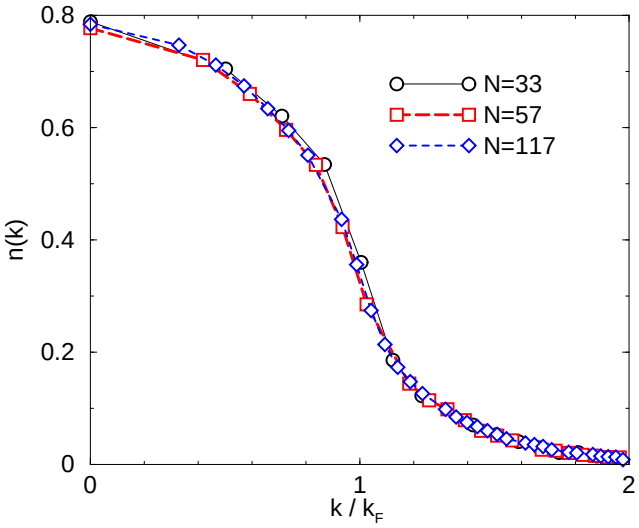

FIG. 9: Finite size study of the momentum distribution for spin polarized electron gas at $r_s = 40$ and $T_F/T = 8$ computed using the variational density matrix method for $N = 33$, 57, and 117 particles in periodic boundary conditions.

dependent Jastrow factor derived from the random phase approximation [8]. However, for the unpolarized system, VDM predicts $n(k)$ values that are significantly too high for $k < k_F$. While the VDM method can certainly be improved by choosing parameters in the Jastrow factor [8] more appropriately, it underlines the need for methods that work without input from analytical calculations.

To estimate the finite size effects, we used the VDM method which is significantly less computationally demanding than PIMC. Fig. 9 shows the finite size dependence of the momentum distribution for the spin polarized electron gas at $r_s = 40$ and $T_F/T = 8$, a density at which PIMC and VDM agree well. The simulations were performed for different numbers of particles corresponding to filled k shell structures with $N = 33$, 57, and 117 particles. Using periodic boundary conditions, the function $n(k)$ can only be computed for k values in the reciprocal lattice of the simulation cell. Consequently, $n(k)$ is shown for a different set of k values depending on the number of particles. The overall agreement of the computed momentum distribution is very good, indicating that the finite size errors are small at these temperatures.

IV. CONCLUSIONS

This computational technique allows one to calculate the momentum distribution within PIMC for fermion systems. It combines the sampling methods using open paths developed for bosonic liquids with restricted path technique derived for fermions. Results for the homogeneous electron gas show that the temperature dependence of the momentum distribution can be studied and ground state results can be reproduced. The method is applicable to any Fermi system, in particular to hot dense hydrogen [11] where one expects significant changes in the momentum distribution with increasing density as the electrons are delocalized in the molecular-metallic transition, and to calculate the momentum distribution of ^{3}He [12] and ^{3}He-^{4}He mixtures.

Acknowledgments

The authors acknowledge useful discussions with J. Shumway. This work was performed in part under the auspices of the U.S. Dept. of Energy at the University of California/Lawrence Livermore National Laboratory under contract no. W-7405-Eng-48 and by NSF -DMR01-04399.

[1] D. M. Ceperley. *Rev. Mod. Phys.*, 67:279, 1995.
[2] D. M. Ceperley. *J. Stat. Phys.*, 63:1237, 1991.
[3] D. M. Ceperley. *Phys. Rev. Lett.*, **69**:331, 1992.
[4] D. M. Ceperley. In Ed. K. Binder and G. Ciccotti, editors, *Monte Carlo and Molecular Dynamics of Condensed Matter Systems*. Editrice Compositori, Bologna, Italy, 1996.
[5] B. Militzer and E. L. Pollock. *Phys. Rev. E*, 61:3470, 2000.
[6] B. Militzer and E. L. Pollock. *Phys. Rev. Lett.*, 89:280401, 2002.
[7] A. B. Migdal. *JETP*, 5:333, 1957.
[8] E. L. Pollock. Finite temperature electron gas correlation energies from a trial density matrix. *Phys. Rev. B*, submitted.
[9] F. H. Zong, C. Lin, and D. M. Ceperley. *Phys. Rev. E*, 66:036703, 2002.
[10] G. Ortiz and P. Ballone. *Phys. Rev. B*, 50:1391, 1994.
[11] S.T. Weir, A.C. Mitchell, and W.J. Nellis. *Phys. Rev. Lett.*, 76:1860, 1996.
[12] R. Senesi, C. Andreani, D. Colognesi, A. Cunsolo, and M. Nardone. *Phys. Rev. Lett.*, 86:4584, 2001.